Materials Horizons

ROYAL SOCIETY OF CHEMISTRY

COMMUNICATION

View Article Online
View Journal | View Issue

Check for updates

Cite this: *Mater. Horiz.*, 2020, 7, 905

Received 18th October 2019,
Accepted 25th November 2019

DOI: 10.1039/c9mh01660k

rsc.li/materials-horizons

Controllable 3D plasmonic nanostructures for high-quantum-efficiency UV photodetectors based on 2D and 0D materials†

Ming-Yu Li,[ab] Muni Yu,[a] Shenglin Jiang,[ab] Sisi Liu,[a] Hezhuang Liu,[c] Hao Xu,[cd] Dong Su,[a] Guangzu Zhang,*[ab] Yuntian Chen[a] and Jiang Wu*[cd]

The confinement of incident light waves for light–matter interactions, especially for 2D materials with axially limited areas, commonly limits the development of high-performance photodetectors with a wide range of semiconductors in the nanoscale. Herein, we propose an approach to spatially extend the light confinement effect from 2D to 3D with Au nanostructure/anodic aluminum oxide (AAO) matrix plasmonic architectures. The incident light beams were initially concentrated by the Au nanostructures (NSs) and the strong plasmon optical interference within AAO matrixes subsequently offered an effective way to trap the light transmitted from the Au NS layers, which was recursively collected by Au NSs. The optical properties of the 3D plasmonic NSs correspondingly exhibited strong morphological dependence, which was evidenced by the tunable intensified Raman vibrational signals of the R6G molecules with a prominent enhancement factor up to 1 × 10^8. As a consequence, the 3D plasmonic nanostructures can be successfully applied in various dimensional materials and overcome the limited solar energy utilization for the ultra-thin 2D *p*-MSB nanoribbons, resulting in a high quantum efficiency up to 1068% under 0.5 mW cm^{-2} UV light illumination.

New concepts

Herein, we propose a new perspective for breakthrough in the spatial light utilization of multiple-dimensional materials applied in photodetectors with configuration-tunable 3D plasmonic nanostructures. Incident light was initially concentrated by the self-assembled Au nanostructures on AAO matrixes and the escaped photons were collected due to multiple couplings within the 3D plasmonic nanostructures, resulting in a morphology-dependent light scattering with a super high enhancement factor (EF) of 1 × 10^8 for R6G molecules. The versatility and accessibility of the 3D plasmonic nanostructures were evidenced by the significantly boosted light absorption of various photoactive materials from typical 0D ZnO quantum dots to new 2D organic *p*-MSB nanoribbons, and the performance of UV photodetectors was enhanced accordingly. There was an increase in photoresponsivity by over one order of magnitude and there was super high quantum efficiency, up to 1068%, under weak light illumination (0.5 mW cm^{-2}). The 3D plasmonic nanostructures hold great promise for achieving ultra-sensitive photodetection for a wide range of photoactive materials with excellent universality.

Introduction

Photodetectors convert incident photons into electrical signals for detection, and the conversion efficiency can be inherently determined by the absorbance of the photoactive layers. Owing to the low interference from the environment, UV photodetectors are highly desirable in military or civilian applications, such as flame detection,[1] inter-satellite communication,[2] ozone hole monitoring,[3] and air and water sterilization.[4] Two-dimensional (2D) materials can potentially act as promising materials for UV photodetector fabrication on various substrates with high responsivity, fast response speed, and less lattice constant mismatch,[5] which are ascribed to the strong light–matter interaction, ultrathin thickness along the vertical direction, and out-of-plane van der Waals bindings.[6] However, 2D materials commonly suffer from a complex fabrication process and limited light utilization due to the non-negligible loss of the incident light *via* transmission, which can inevitably deteriorate the performance of the photodetectors. The occurrence of a 2D organic semiconductors, *i.e.*, 1,4-bis(4-methylstyryl)benzene (*p*-MSB) with low-cost solution processability, high flexibility, and tailored band structures can fundamentally break the barriers of the fabrication for 2D material-based new-generation high-performance UV

---

[a] *School of Optical and Electronic Information and Wuhan National Laboratory of Optoelectronics, Huazhong University of Science and Technology, Wuhan, Hubei 430074, China. E-mail: zhanggz@hust.edu.cn*
[b] *Shenzhen Huazhong University of Science and Technology Research Institute, Shenzhen, Guangdong, 518057, China*
[c] *Institute of Fundamental and Frontier Sciences, University of Electronic Science and Technology of China, Chengdu, Sichuan 610054, China. E-mail: jiangwu@uestc.edu.cn*
[d] *Department of Electronic and Electrical Engineering, University College London, London, WC1E 6BT, UK*

† Electronic supplementary information (ESI) available. See DOI: 10.1039/c9mh01660k

photodetectors.[7] Meanwhile, ZnO colloidal quantum dots (QDs) have been regarded as typical candidates with an appropriate bandgap (3.37 eV) and high exciton binding energy (60 meV) for low-cost UV photodetector fabrication;[8] they have attracted significant research interest to enhance the performance of ZnO QD-based detectors.

To enhance the quantum efficiency, efforts have been made to utilize the nano-confinement effect to trap the incident light within the nanostructure arrays, including nanowires,[9] nanoflakes,[10] and nanorods.[11] Nevertheless, the insufficient effective area in the axial-direction and discrete morphology have severely restricted the efficiency and response speed of the nanostructure array-based photodetectors. Owing to the resonant collective oscillation of the electrons on the metallic nanostructures (NSs), the boosted near-surface electromagnetic (EM) field presents another way to concentrate the incident light,[12] which can still be restricted in the areas with metallic NSs. Herein, we propose that novel 3D plasmonic NSs can spatially concentrate the incident light, offering a facile method to break through the light utilization limitation for UV photodetection in a wide range of photoactive materials. By systematically controlling the evolution of the self-assembled Au NSs from hemispherical nanoparticles (NPs) to coralline nano-mounds (NMs) on the AAO matrixes, drastic development in the plasmonic optical interference was successfully achieved within 3D plasmonic NSs, which was verified with a drastically enhanced enhancement factor (EF) of 1 × 10^8 for the R6G molecules. With the existence of such configurable 3D plasmonic structures, the light utilization of the 2D *p*-MSB nanoribbons and ZnO QDs was radically boosted under the influence of a significantly intensified EM field, resulting in a distinctly improved performance. There was an increase in photoresponsivity by over one order of magnitude and super high quantum efficiency up to 1068% under weak light illumination (0.5 mW cm^{-2}).

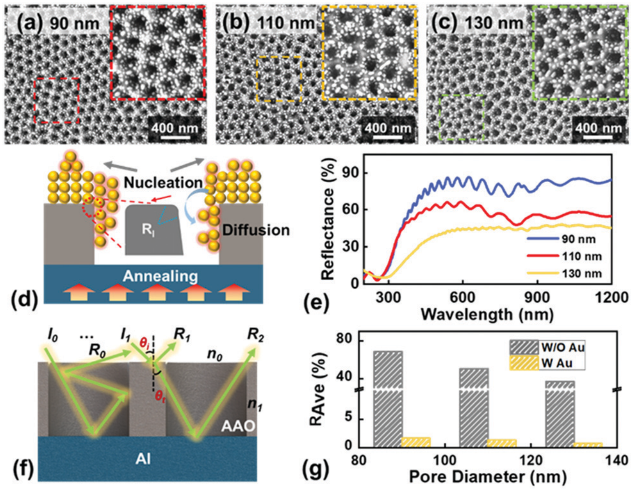

Fig. 1 SEM images of the self-assembled Au NPs fabricated with 6 nm deposition thickness on AAO/Al substrates with various average pore diameters (D_p): (a) 90, (b) 110, and (c) 130 nm. Inset: The enlarged SEM images of localized morphologies acquired from the area with dashed squares. (d) Scheme of the aggregation of the self-assembled Au NPs; R_l indicates the local curvature radius. (e) Reflectance spectra of the pristine AAO/Al substrates of different D_p. (f) Scheme showing how interference occurred between AAO and Al. I, R, and T indicate incident, reflected, and transmitted optic waves, respectively. θ_i and θ_t denote the incident and transmitted angles, and the refractive indices in air and AAO are denoted by n_0 and n_1. (g) The average reflectance (R_{Ave}) of the AAO/Al substrates of different D_p with and without Au NPs.

Results and discussion

To obtain the plasmonic structures, an AAO matrix was initially prepared by electrochemical etching. A gold thin film was evaporated on the as-etched AAO matrix for the fabrication of Au NSs by thermal annealing. The photoactive layers, *i.e.*, 2D or 0D materials, were finally spin-coated on the as-fabricated plasmonic structures to investigate the plasmonic enchantment. The morphological and optical property evolution of the self-assembled Au NPs fabricated on the AAO/Al substrates as a function of the average pore diameters (D_p) with fixed Au deposition thicknesses of 6 nm is shown in Fig. 1. The Au NPs were evenly distributed on the AAO template, and size expansion of the Au NPs gradually occurred with increasing D_p as shown in Fig. 1a–c. On obtaining thermal energy, the Au adatoms began to aggregate at the matrixes of the AAO template and even tended to diffuse into the pores, minimizing the chemical potential as depicted in the inset in Fig. 1d. According to the Gibbs–Thomson relation,[13] the local excess potential $\Delta\mu$ can be given by

$$\Delta\mu = \frac{1}{R_l}\gamma_{Au}\Omega_{Au}, \tag{1}$$

where R_l indicates the local curvature radius, γ_{Au} is the excitation energy of Au atoms, and Ω_{Au} denotes the atom volume (10.3).[14] With the increasing D_p, the R_l gradually decreased due to the increasing curvature during the etching process, which can result in increased $\Delta\mu$. Therefore, the nucleation of Au atoms had a tendency to occur on the AAO matrixes rather than on the sidewalls, which in turn caused the increase in the average diameter from 30 to 52 nm (Fig. S1, ESI†). As shown in Fig. 1e, regardless of the D_p of the AAO/Al substrates, the interference fringes, well developed below the band gap (~3.2 eV ≈ 390 nm),[15] can be induced by the interference of multiple reflected beams as depicted in Fig. 1f. Given that the reflected light R_n ($n > 2$) can be negligible due to the relatively lower intensity, the superposition of reflected lights waves can be briefly expressed as follows:[16]

$$R(\lambda) = R_1 + R_2 + 2\sqrt{R_1R_2}\cos\frac{4\pi dn_1\cos\theta_i}{\lambda}, \tag{2}$$

where R_1 and R_2 are the first and second reflected beams, θ_i indicates the angle of incident light, n_1 is the refractive index, and d is the thickness of AAO layers of 2 μm. Since the light was severely consumed by scattering among the AAO arrays, the loss factor (α) can be introduced into eqn (2):

$$R(\lambda) = R_1e^{-\alpha} + R_2e^{-\alpha} + 2\sqrt{R_1R_2e^{-2\alpha}}\cos\frac{4\pi dn_1\cos\theta_i}{\lambda}. \tag{3}$$

Here, α can be given by $\alpha = k\frac{\sigma}{\lambda}$,[17,18] where σ is the surface roughness, and k is the fitting constant. Apparently, a relatively higher α can be expected with increased D_p, which was attributed to the increased σ along with the enlarged surface area. As a result, the average reflectance over a wavelength range between 200 and 1200 nm was linearly decreased by ~1.9 times from 69% to 37% as shown in Fig. 1g, suggesting a strong dependence of the D_p on the optical properties. According to previous work, a radical resonant plasmonic coupling[19] can appear between metallic layers and AAO arrays, and the plasmonic optical interference can be significantly boosted with the existence of Au NSs due to the enhanced near-surface EM field.[20] Consequently, the reflectance decreased drastically for each sample with the Au NP-decorated 3D plasmonic NSs over the whole wavelength range (Fig. 1g and Fig. S2, ESI†), which eventually resulted in a reflectance below 1% for the sample with D_p of 130 nm. In addition, AAO layers generally suffer from noticeable transmission[21] and thus, the Al reflection mirror layers can further improve the plasmonic coupling of the Au NPs.

The configuration effects of the Au NSs on the optical properties of the 3D plasmonic NSs are shown in Fig. 2. The surface morphologies of the 3D plasmonic NSs with a variation in the deposition thicknesses between 10 and 15 nm (D_p = 130 nm) are presented in Fig. 2a and b, and the morphological development for other D_p values at each deposition thickness are given in Fig. S3 (ESI†). According to the diffusion-limited agglomeration model,[23] the dewetting rate of Au NSs (ν_{Au}) can be expressed as follows:[24]

$$\nu_{Au} \propto \frac{D_s}{T} \times \frac{1}{h^3}, \tag{4}$$

where D_s is the diffusion coefficient, which can be determined by the annealing temperature (T). Here, the self-assembled NSs were fabricated at a fixed T, and thus, the ν_{Au} can be reduced by increasing the deposition thickness (h), which resulted in an increased surface coverage of the Au NSs. As a result, a radical morphology evolution from the hemispherical NPs to the coralline nano-mounds (NMs) was observed with the increasing h at each D_p as shown in Fig. 2a and b, and additional adatoms began to diffuse into the pores as evidenced in Fig. S4 (ESI†). Meanwhile, due to the increased $\Delta\mu$ with the increasing D_p, additional Au adatoms aggregated on the AAO matrixes rather than diffusing into pores, eventually leading to full coverage of the coralline Au NMs on AAO matrixes as shown in Fig. 2b. The tendency toward Au NS distribution at the AAO matrixes was witnessed *via* the energy dispersive X-ray spectroscopy (EDS) elementary maps in Fig. S5 (ESI†). Depending on the morphology, the reflectance of the 3D plasmonic NSs drastically evolved as functions of the D_p and configuration of the Au NSs as shown in Fig. 2c. With the morphological evolution of the self-assembled Au NSs, the average reflectance (R_{Ave}) initially declined at each D_p, suggesting much more intense plasmonic coupling with the coralline Au NMs.[25] However, at 15 nm, the R_{Ave} slightly increased above ~2% at each D_p due to the reduced light scattering along with the decreased σ, which was induced by the damped EM field when the AAO matrixes were almost covered with the coralline NMs.

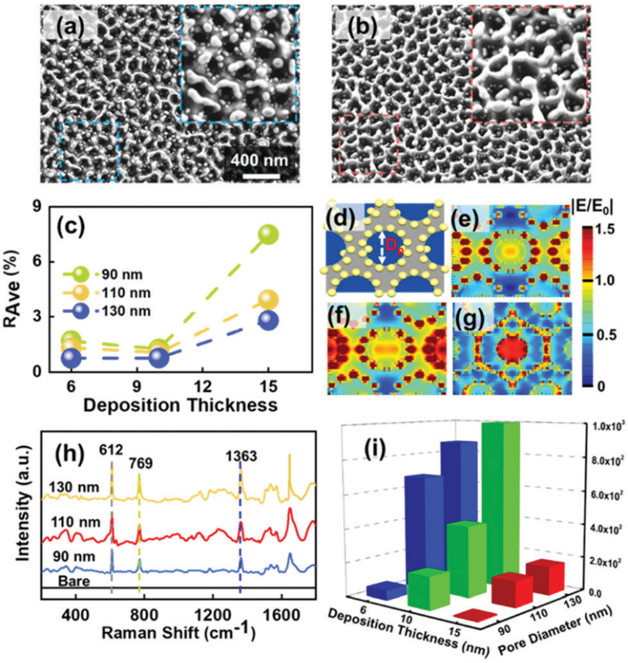

Fig. 2 SEM images of the self-assembled Au NSs fabricated on AAO/Al substrates with an identical D_p of 130 nm. The deposition thicknesses were (a) 10 and (b) 15 nm. (c) The R_{Ave} over a wavelength range between 200 and 1200 nm. (d) Scheme of the Au NSTs/AAO/Al 3D plasmonic NSs for FDTD simulation. The electromagnetic (EM) field distribution simulation of 3D plasmonic with various Au NSs: (e) Au NPs (D_p = 90 nm), (f) Au NPs (D_p = 110 nm), (g) coralline Au nano-mounds (D_p = 110 nm). (h) Raman spectra of R6G molecules on the 3D plasmonic NSs with various D_p. (i) Enhancement factor (EF) of all the samples.

To explain the morphology-dependent light confinement effect, the electromagnetic (EM) field distribution of the 3D plasmonic NSs with various D_p and Au NSs was evaluated *via* the finite-different time-domain (FDTD) simulation method. As shown in Fig. 2e and f, the surface EM field was obviously boosted with the increased D_p from 90 to 110 nm. With an identical D_p of 110 nm, the EM field was correspondingly damped when the Au NSs evolved from the hemispherical NPs to the coralline NMs, as shown in Fig. 2f and g. In addition, R6G molecules were employed as analytes to verify the plasmonic optical interference of 3D plasmonic NSs. Under 532 nm laser excitation, the pronounced Raman bands at 612, 769, and 1363 cm^{-1} were due to the characteristic peaks of R6G molecules, which can be attributed to the C–C–C ring in-plane and out-of-plane bending, and aromatic C–C symmetric stretching of the xanthene ring vibration modes.[22] Compared with the bare glass, Raman signals of the R6G molecules on the 3D plasmonic NSs were prominently enhanced regardless of the D_p, as shown in Fig. 2h and Fig. S6 (ESI†), indicating strong light excitation due to the plasmonic optical interference within the 3D plasmonic NSs. Depending on the D_p, the intensities of the peaks at 612 and 1363 cm^{-1} gradually increased by 91% and 26% with the expanded D_p (Table S1, ESI†), respectively. The enhancement factors (EF) of the 3D plasmonic NSs for the peak at 1363 cm^{-1} are revealed in Fig. 2(i). The EF constantly increased as a function of the D_p, and the maximum EF of 1×10^8 was obtained on the 3D plasmonic NSs with a D_p of 130 nm when the deposition thickness was 10 nm. At 15 nm, the Raman peaks increased initially and eventually decreased with the increasing D_p, which was probably induced by the gradually reduced Au NMs for the R6G molecules.[26]

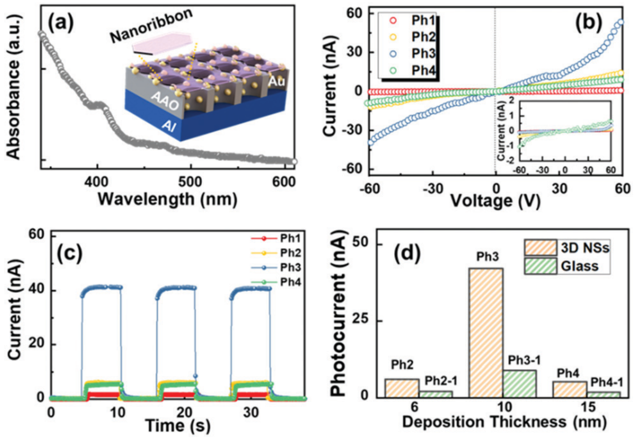

Fig. 3 Performance of the *p*-MSB nanoribbon/3D plasmonic NSs photodetectors (D_p = 130 nm) with various Au deposition thicknesses: 6 (Ph2), 10 (Ph3), and 15 nm (Ph4). Ph1 indicates the device with *p*-MSB nanoribbons grown on glass. (a) The absorbance spectra of *p*-MSB nanoribbons. (b) *I*–*V* curves of each device under 365 nm UV light illumination (6.9 mW cm^{-2}). (Inset) *I*–*V* curves of the devices in the dark. (c) Time-resolved UV photoresponses of the devices under UV light illumination. (d) Photocurrents of the devices with the Au NSs fabricated on AAO/Al substrates and glass at each deposition thickness. The devices fabricated on glass: Ph2-1 (6 nm), Ph3-1 (10 nm), and Ph4-1 (15 nm).

Overall, the 3D plasmonic NSs exhibited an outstanding enhancement effect as compared to other nanostructures as shown in Table S2 (ESI†), indicating that the 3D plasmonic NSs have great potential to concentrate the incident light for the absorption of the analytes.

To further investigate the enhancement effect, the 2D organic *p*-MSB ribbons were employed for the fabrication of photodetectors on the 3D plasmonic NSs with various Au NSs at an identical D_p of 130 nm and on bare glass (Ph1) as shown in Fig. 3 and 4. Depending on the deposition thicknesses for the Au NS fabrication, the devices were denoted as Ph2 (6 nm), Ph3 (10 nm), and Ph4 (15 nm). The absorbance spectra of *p*-MSB nanoribbons are shown in Fig. 3a, exhibiting a relatively broadened absorption band up to 440 nm. As shown in Fig. 3(b), the dark current (I_{Dark}) of the *p*-MSB ribbons grown on each substrate was comparable, and the photocurrent (I_{Ph}) of the *p*-MSB/3D plasmonic NSs photodetectors was obviously enhanced at each bias under 365 nm light illumination even with 3 layers (6.3 nm) of *p*-MSB as evidenced by atomic force microscope (AFM) top-views (Fig. S7, ESI†). As shown in Fig. 3b, the I_{Ph} gradually developed with the morphological evolution of the 3D plasmonic NSs, and thus, the I_{Ph} of Ph3 significantly increased by $\sim$23 times as summarized in Table S3 (ESI†). Notably, each photodetector responded similarly to the incident light within 0.3 s, suggesting the ultra-fast speed of the photodetectors even with 3D plasmonic NSs. In order to confirm the role of the AAO matrixes, the *p*-MSB ribbons were grown on the glass with the various Au NSs fabricated within an identical variation of deposition thicknesses: Ph2-1 (6 nm), Ph3-1 (10 nm), and Ph4-1 (15 nm).

The comparison of photocurrent for the devices is shown in Fig. 3(d), and the performance of the devices fabricated on glass is presented in Fig. S8 (ESI†). The I_{ph} was significantly enhanced for the Au NSs with the existence of the AAO matrixes, which suggested that the AAO matrixes played a crucial role in the improved performance. The responsivity of the devices (*R*) indicates the ability to generate photocurrent under an identical light intensity ($\Delta I = I_{Ph} - I_{Dark}$), which can be given as follows:[27]

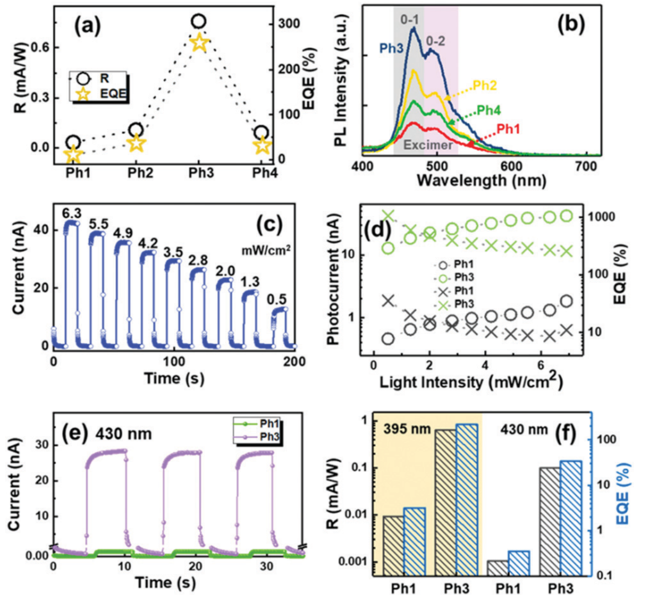

Fig. 4 (a) Photoresponsivity (*R*), external quantum efficiency (EQE) and (b) photoluminescence (PL) spectra for the *p*-MSB nanoribbon/3D plasmonic NSs photodetectors (D_p = 130 nm). (c) Photoresponse of the Ph3 at various light intensities under 365 nm light illumination. (d) Photocurrent and EQE of each device under varied illumination powers. The circle indicates the photocurrent, and the cross denotes the EQE. (e) Time-resolved photoresponse of Ph1 and Ph3 under 430 nm light illumination. (f) *R* and EQE of the devices Ph1 and Ph3 under 395 and 430 nm light illumination.

$$R = \frac{\Delta I}{PA}, \tag{5}$$

where *P* and *A* represent the illumination power (6.9 mW cm^{-2}) and the area between two electrodes of 0.2 × 4 mm^2. The *R* of the *p*-MSB/3D plasmonic NS photodetectors was pronounceably enhanced along with the morphological evolution, resulting in a maximum *R* of $\sim$0.76 mA W^{-1} for the device Ph3 (Fig. 4a). Besides, the external quantum efficiency (EQE) of the photodetectors can be expressed as[28]

$$\mathrm{EQE} = \frac{R \times 1240}{\lambda} \times 100\% \tag{6}$$

where λ is the exciting wavelength (365 nm). With the existence of the 3D plasmonic NSs, the EQE was radically increased, resulting in a 25-time increase up to 258% for device Ph3. The 0–1 band at 460 nm and 0–2 band at 490 nm[29] in the photoluminescence (PL) spectra gradually increased (Fig. 4b), indicating a radically intensified excitation for carrier generation.

As shown in Fig. 4c, the I_{Ph} of device Ph3 sensitively responded to the incident light power from 6.3 to 0.5 mW cm^{-2}. Interestingly, the EQE of device Ph3 was enhanced by 30 times to 1068% when the light intensity was 0.5 mW cm^{-2} (Fig. 4d);

i.e., the sensitivity of the incident photons of the photodetector can be effectively enhanced by 3D plasmonic NSs even under weak light illumination. In addition, the response of the photodetector can be effectively enhanced within a wide range, even up to 430 nm, as shown in Fig. 4e and Fig. S9 (ESI†). As shown in Fig. 4f, radical increases up to 100 times were correspondingly observed in R and EQE at 430 nm (Fig. 4f), suggesting a facile way to broaden the response wavelengths.

The ZnO QDs were spin-coated on bare glass (Ph5) and the 3D plasmonic NSs with varied deposition thicknesses for Au NS fabrication: Ph6 (6 nm), Ph7 (10 nm), and Ph8 (15 nm). Similar to the 2D materials, the I_{Ph} of the photodetectors fabricated on the 3D plasmonic NSs was remarkably enhanced at each bias voltage (Fig. 5b). Under UV light illumination (6.9 mW cm^{-2}), the I_{ph} of device Ph7 steadily reached a value of ~36 μA with a bias of 10 V (Fig. 5c), which was a significant enhancement (~36 times) as compared with the device Ph5, even with identical thickness of ZnO layers (Fig. S10, ESI†). The Au NSs were fabricated under identical conditions on glass to further prove the enhancement effect *via* the plasmonic optical interference as shown in Fig. 5d and Fig. S11 (ESI†): Ph6-1 (6 nm), Ph7-1 (10 nm), and Ph8-1 (15 nm). With the existence of AAO matrixes, I_{ph} was radically increased for various Au NSs, and the dark current was simultaneously restricted due to the reduced area of the Au NSs. Meanwhile, each photodetector showed fast response to the incident light within ~3 s (Fig. S12 and Table S4, ESI†).

Nevertheless, the decay time of the photodetectors fabricated on the 3D plasmonic NSs was slightly slower, which was probably induced by the increased electron collection paths with the existence of the Au NSs.[30,31] As a result, the R and EQE of the ZnO/3D plasmonic NS photodetectors gradually developed in light of the morphological evolution of the NSs, and the optimized R and EQE reached ~0.66 A W^{-1} and 225% for device Ph7 (Fig. 6a), respectively. For device Ph8, R decreased to ~0.12 A W^{-1} due to the damped plasmonic coupling, which was still one order higher than that of Ph5. Compared with the Au nanoantenna-based ZnO photodetectors in previous work,[32–36] the EQE was also dramatically enhanced by 3 times (Table 1), suggesting that the 3D plasmonic NSs can vastly promote charge carrier generation by the incident photons, owing to the plasmonic light coupling. As shown in Fig. 6b, there is a near-band-edge (NBE) emission peak at 370 nm[37] and the radiative recombination of electron–hole pairs from ZnO occurred similarly for each device. In principle, the excitation of the electrons from ZnO can happen more thoroughly for the devices fabricated on the 3D plasmonic structures due to the intensified incident light, which can potentially enhance the radiative recombination. However, the generated charge carriers can be trapped by the Au NSs due to the enhanced surface EM fields,[38] which suppressed the recombination for the NBE emission. Meanwhile, the defect level emissions in the visible region were intensified with the existence of the 3D plasmonic NSs, manifesting a much more noticeable resonant light coupling in the intrinsic excitation regions of Au NSs.[39] Additionally, the I_{ph} of device Ph7 was obviously higher than that of device Ph5 at each illumination power between 1.35 and 6.9 mW cm^{-2}, as shown in Fig. 6c. It is worth noting that the I_{ph} of device Ph7 radically increased by one order with the elevated light intensity, suggesting a very sensitive response to the illumination power owing to the enhanced excitation of the carriers as the result of light coupling within the 3D plasmonic NSs. Correspondingly, R also responded sensitively to the illumination intensity of the excitation light as shown in Fig. 5d, which indicated that light sensitivity can be effectively improved by introducing 3D plasmonic NSs.

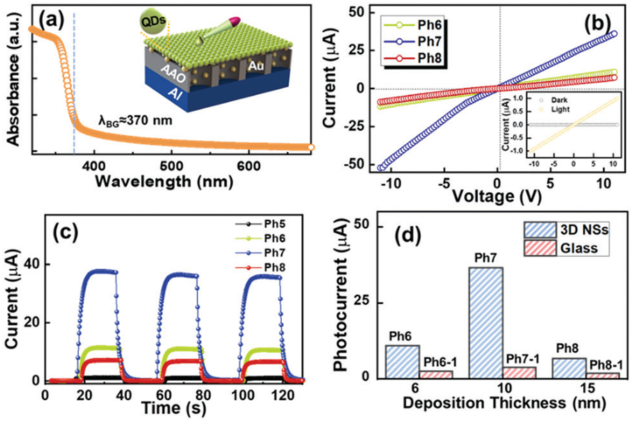

Fig. 5 Performance of the ZnO/3D plasmonic NSs photodetectors (D_{p} = 130 nm), and the Au NSs fabricated at 6 (Ph6), 10 (Ph7), and 15 nm (Ph8). (a) Absorbance spectra of ZnO CQDs. (b) Photocurrent at each bias of each device under 365 nm UV light illumination (6.9 mW cm^{-2}). Inset: Photocurrent and dark current of the ZnO photodetector on glass (Ph5) at each bias. (c) Time-resolved photoresponse of the ZnO photodetectors under UV light illumination (6.9 mW cm^{-2}). (d) Photocurrents of the devices with the Au NSs fabricated on AAO/Al substrates and glass at each deposition thickness. The devices fabricated on glass: Ph6-1 (6 nm), Ph7-1 (10 nm), and Ph8-1 (15 nm).

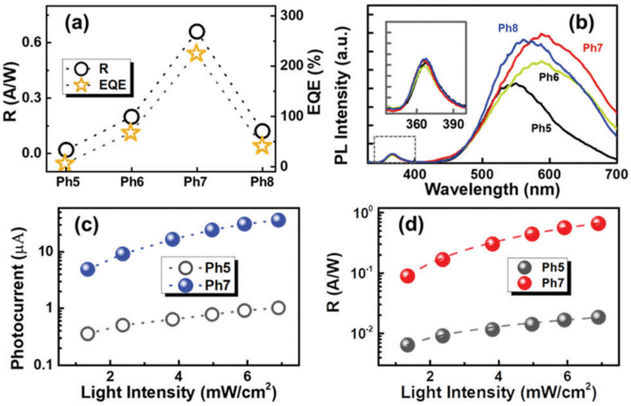

Fig. 6 (a) Photoresponsivity (R), external quantum efficiency (EQE) and (b) PL spectra for all ZnO samples. Illumination power-dependent (c) photocurrent and (d) EQE of the photodetectors Ph5 and Ph7.

Conclusions

In conclusion, we have provided a widely applicable solution to boost the light utilization for UV high-performance photodetection

Table 1 Comparison of the characteristic photoresponse parameters of the photodetectors reported in the literature

Material	Light source	I_{ph} (μA)	R (mA W^{-1})	t_{rise} (s)	t_{decay} (s)	EQE (%)
ZnO/graphene nanodot arrays[32]	300 nm	4.33×10^{-2}	22.55	2.5	11	9.32
ZnO homojunction nanofibers[33]	360 nm, 2.5 mW cm^{-2}	0.5×10^{-3}	1	3.9	4.7	—
ZnO/CdO nanofibers[34]	300 nm, 6.54 mW cm^{-2}	<1	10^3	4	3	—
Au NPs/$CdMoO_4$ microplates/ZnO film[35]	350 nm, 450 W	2.89×10^{-1}	321.1	16	9.2	—
ZnO/Au nanoantennas[36]	365 nm	12.78	231.47	3.55	1.49	78.8
Ph7	365 nm	36.59	661.01	2	4	225.13

with topology-controllable 3D plasmonic NSs due to a spatially tunable light confinement effect. Depending on the D_p, the size expansion of Au NSs was similarly witnessed as a function of the AAO pore diameter due to increased $\Delta\mu$, indicating the development of preferential nucleation sites for the Au NSs. Meanwhile, the self-assembled Au NSs evolved radially from the hemispherical NPs to the coralline NMs with increasing deposition thickness based on the diffusion-limited agglomeration model. Hence, the incident light beams were successfully confined within the 3D plasmonic NSs owing to the strong plasmon optical interference, and surface scattering was inherently varied as a function of the topology caused by the variation in light coupling, which was theoretically discussed with the varied EM field distribution. The coupling effect was confirmed with enhanced Raman vibrational modes of the R6G molecules, and a surface morphology dependent EF was eventually reached at 1×10^8. As a consequence, the performance of the photodetectors fabricated on the 3D plasmonic NSs was drastically improved and sharply varied with the geometry of the 3D NSs, manifesting a novel and controllable method for breakthrough in the limitation of the performance of the UV photodetectors rather than the simple variations of materials.

Experimental section

Preparation of 3D plasmonic NSs

A highly ordered porous AAO template on Al substrate was adapted to fabricate the 3D plasmonic NSs, which were prepared by the two-step anodization technique[40] (detailed description in ESI†). The as-etched AAO/Al substrates were highly uniform with an inter-pore distance of ~140 nm, and the average pore diameters of AAO/Al substrates were 90, 110, and 130 nm. To investigate the deposition thickness effect, the AAO/Al substrates were deposited with varied thicknesses of Au thin films (T_{Au}) between 6 and 15 nm *via* thermal evaporation at a rate of 0.1 nm s^{-1} under $\sim 7 \times 10^{-4}$ Pa. The Au NSs were subsequently fabricated by annealing at 500 °C for 900 s in a rapid thermal annealing furnace under 1×10^{-5} Pa, and then directly quenched to room temperature.

Fabrication of the 3D plasmonic NSs associated photodetectors

For the *p*-MSB-based photodetectors, the *p*-MSB nanoribbons were deposited on substrates *via* drop-casting methods[41] (detailed description of the synthesis of the *p*-MSB seeds in ESI†). The *p*-MSB seeds were ~10 μm in width and ~20 μm in length (Fig. S12a, ESI†), and could avoid collapse into AAO pores during the *p*-MSB nanoribbon growth. The selected-area electron diffraction (SAED) patterns were a single set of spots (Fig. S12b, ESI†), indicating the preferential growth of *p*-MSB nanoribbons along the [010] and [100] directions.[42] To evaluate the enhancement effect of the 3D plasmonic NSs, 100 mL of saturated *p*-MSB solution was cast on the 3D plasmonic NSs (D_p = 130 nm) with T_{Au} of 6 nm (Ph2), 10 nm (Ph3), and 15 nm (Ph4). For comparison, an identical amount of *p*-MSB solution was dropped on glass (Ph1). During casting, each sample was annealed at 100 °C to enhance the lateral crystallization, and the samples were subsequently annealed at 80 °C under N_2 in a glove box to evaporate the solvent. For the ZnO-based photodetectors, ZnO CQDs were initially synthesized by the solvothermal method as described in our previous work[36] (detailed description in ESI†). The wurtzite ZnO was evidenced by lattice fringes with interplanar spacing of 0.26 nm and 0.24 nm, corresponding to (002) and (101) crystal planes (Fig. S12c, ESI†). The six diffraction rings in the SAED pattern indicated a high degree of crystallinity (Fig. S12d, ESI†), suggesting a high preference for favourable quality film fabrication. The ZnO CQDs films were spin-coated layer by layer at 2000 rpm for 40 s on 3D plasmonic NSs (D_p = 130 nm) and bare glass as reference. Depending on the T_{Au}, the photodetectors were denoted as Ph5 (ZnO on bare glass), Ph6 (T_{Au} = 6 nm), Ph7 (T_{Au} = 10 nm), and Ph8 (T_{Au} = 15 nm). Each sample was subsequently annealed at 250 °C for 1 h in a tube furnace.

Conflicts of interest

There are no conflicts to declare.

Acknowledgements

This research was supported by the National Natural Science Foundation of China (Grant No. 61705070, 61675076, 51772108), the China Postdoctoral Science Foundation (Grant No. 2017M612449 and 2017T200545), and the Shenzhen Science and Technology Project (Grant No. JCYJ20180507182248925). We also would like to acknowledge the Analytical and Testing Center of Huazhong University of Science and Technology.

References

1 H. Chen, K. Liu, L. Hu, A. Al-Ghamdi and X. Fang, *Mater. Today*, 2015, **18**, 493.
2 X. Liu, L. Gu, Q. Zhang, J. Wu, Y. Long and Z. Fan, *Nat. Commun.*, 2014, **5**, 4007.

3 H. Chen, P. Yu, Z. Zhang, F. Teng, L. Zheng, K. Hu and X. Fang, *Small*, 2016, **12**, 5809.

4 H. Chen, H. Liu, Z. Zhang, K. Hu and X. Fang, *Adv. Mater.*, 2016, **28**, 403.

5 J. Chu, F. Wang, L. Yin, L. Lei, C. Yan, F. Wang, Y. Wen, Z. Wang, C. Jiang, L. Feng, J. Xiong, Y. Li and J. He, *Adv. Funct. Mater.*, 2017, **27**, 1701342.

6 N. Huo and G. Konstantatos, *Adv. Mater.*, 2018, **30**, 1801164.

7 Y. Liu, S. Zhang, J. He, Z. M. Wang and Z. Liu, *Nano-Micro Lett.*, 2019, **11**, 13.

8 Y. Ning, Z. Zhang, F. Teng and X. Fang, *Small*, 2018, **14**, 1703754.

9 L. Li, L. Gu, Z. Lou, Z. Fan and G. Shen, *ACS Nano*, 2017, **4**, 4067.

10 X. Z. Li, J. Xia, L. Wang, Y. Y. Gu, H. Q. Cheng and X. M. Meng, *Nanoscale*, 2017, **9**, 14558.

11 V. Q. Dang, T. Q. Trung, D. I. Kim, L. T. Duy, B. U. Hwang, D. W. Lee, B. Y. Kim, L. D. Toan and N. E. Lee, *Small*, 2015, **11**, 3054.

12 H. Thilsted, J. Y. Pan, K. Y. Wu, K. Zór, T. Rindzevicius, M. S. Schmidt and A. Boisen, *Small*, 2016, **12**, 6745.

13 H. Jo, D. Yoon, A. Sohn, D. W. Kim, Y. Choi, T. Kang, D. Choi, S. W. Kim and L. P. Lee, *J. Phys. Chem. C*, 2014, **118**, 18659.

14 E. Yablonovitch and T. J. Gmitter, *Phys. Rev. Lett.*, 1989, **63**, 1950.

15 S. Chakrabarti, R. Panja, S. Roy, A. Roy, S. Samanta, M. Dutta, S. Ginnaram, S. Maikap, H. M. Cheng, L. N. Tsai, Y. L. Chang, R. Mahapatra, D. Jana, J. T. Qiu and J. R. Yang, *Appl. Surf. Sci.*, 2018, **433**, 51.

16 X. X. Huo, S. L. Jiang, P. Liu, M. Shen, S. Y. Qiu and M. Y. Li, *CrystEngComm*, 2017, **19**, 4413.

17 H. M. Branz, V. E. Yost, S. Ward, K. M. Jones, B. To and P. Stradins, *Appl. Phys. Lett.*, 2009, **94**, 231121.

18 Z. C. Feng, T. R. Yang and Y. T. Hou, *Mater. Sci. Semicond. Process.*, 2001, **4**, 571.

19 D. Choi, C. K. Shin, D. Yoon, D. S. Chung, Y. W. Jin and L. P. Lee, *Nano Lett.*, 2014, **14**, 3374.

20 L. Dong, X. Yang, C. Zhang, B. Cerjan, L. Zhou, M. L. Tseng, Y. Zhang, A. Alabastri, P. Nordlander and N. J. Halas, *Nano Lett.*, 2017, **17**, 5768.

21 Y. E. Silina, T. A. Kychmenko and M. Koch, *Anal. Methods*, 2016, **8**, 45.

22 C. Zhang, P. Yi, L. Peng, X. Lai, J. Chen, M. Huang and J. Ni, *Sci. Rep.*, 2017, **7**, 39814.

23 M. Y. Li, Q. Zhang, P. Pandey, M. Sui, E. S. Kim and J. Lee, *Sci. Rep.*, 2016, **6**, 24470.

24 S. Kunwar, M. Sui, Q. Zhang, P. Pandey, M. Y. Li and J. Lee, *Nano-Micro Lett.*, 2017, **9**, 17.

25 S. J. Kwon, G. Y. Lee, K. Jung, H. S. Jang, J. S. Park, H. Ju, I. K. Han and H. Ko, *Adv. Mater.*, 2016, **28**, 7899.

26 R. Yan, Y. Zhao, H. Yang, X. J. Kang, C. Wang, L. L. Wen and Z. D. Lu, *Adv. Funct. Mater.*, 2018, **28**, 1802021.

27 Y. Z. Chen, S. W. Wang, T. Y. Su, S. H. Lee, C. W. Chen, C. H. Yang, K. Wang, H. C. Kuo and Y. L. Chueh, *Small*, 2018, **14**, 1704052.

28 L. Li, F. Zhang, J. Wang, Q. An, Q. Sun, W. Wang, J. Zhang and F. Teng, *Sci. Rep.*, 2015, **5**, 9181.

29 X. Wang, H. Li, Y. Wu, Z. Xu and H. Fu, *J. Am. Chem. Soc.*, 2014, **136**, 16602.

30 M. Sun, Z. Xu, M. Yin, Q. Lin, L. Lu, X. Xue, X. Zhu, Y. Cui, Z. Fan, Y. Ding, L. Tian, H. Wang, X. Chen and D. Li, *Nanoscale*, 2016, **8**, 8924.

31 A. Chaaya, M. Bechelany, S. Balme and P. Miele, *J. Mater. Chem. A*, 2014, **2**, 20650.

32 R. Tang, S. Han, F. Teng, K. Hu, Z. Zhang, M. Hu and X. Fang, Size-Controlled Graphene Nanodot Arrays/ZnO Hybrids for High-Performance UV Photodetectors, *Adv. Sci.*, 2018, **5**, 1700334.

33 Y. Ning, Z. Zhang, F. Teng and X. Fang, Novel Transparent and Self-Powered UV Photodetector Based on Crossed ZnO Nanofiber Array Homojunction, *Small*, 2018, **14**, 1703754.

34 Z. Zheng, L. Gan, H. Li, Y. Ma, Y. Bando, D. Golberg and T. Zhai, A Fully Transparent and Flexible Ultraviolet-Visible Photodetector Based on Controlled Electrospun ZnO-CdO Heterojunction Nanofiber Arrays, *Adv. Funct. Mater.*, 2015, **25**, 5885.

35 W. Ouyang, F. Teng, M. Jiang and X. Fang, ZnO Film UV Photodetector with Enhanced Performance: Heterojunction with CdMoO4 Microplates and the Hot Electron Injection Effect of Au Nanoparticles, *Small*, 2017, **13**, 1702177.

36 S. Liu, M. Y. Li, D. Su, M. Yu, H. Kan, H. Liu, X. Wang and S. Jiang, Broad-Band High-Sensitivity ZnO Colloidal Quantum Dots/Self-Assembled Au Nanoantennas Heterostructures Photodetectors, *ACS Appl. Mater. Interfaces*, 2018, **10**, 32526.

37 F. Xue, L. Chen, J. Chen, J. Liu, L. Wang, M. Chen, Y. Pang, X. Yang, G. Gao, J. Zhai and Z. L. Wang, *Adv. Mater.*, 2016, **28**, 3391.

38 S. K. Soo, A. T. Le, S. Y. Pung, S. Sreekantan, A. Matsuda and D. P. Huynh, *Appl. Phys. A: Mater. Sci. Process.*, 2018, **124**, 783.

39 W. Chamorro, J. Ghanbaja, Y. Battie, A. E. Naciri, F. Soldera, F. Mücklich and D. Horwat, *J. Phys. Chem. C*, 2016, **120**, 29405.

40 E. Choudhar and V. Szalai, *RSC Adv.*, 2016, **6**, 67992.

41 M. Cao, C. Zhang, Z. Cai, C. Xiao, X. Chen, K. Yi, Y. Yang, Y. Lu and D. Wei, *Nat. Commun.*, 2019, **10**, 756.

42 M. Cao, Z. Cai, X. Chen, K. Yi and D. Wei, *J. Mater. Chem. C*, 2017, **5**, 9597.